Supplementary Information

Nanoindentation cannot accurately predict the tensile strength of graphene or other 2D materials

Jihoon Han [a,b], Nicola Pugno [c,d,e], and Seunghwa Ryu [a,*]

[a] Department of Mechanical Engineering, Korea Advanced Institute of Science and Technology (KAIST), 291 Daehak-ro, Yuseong-gu, Daejeon, 305-701, Republic of Korea
[b] Research Reactor Utilization Department, Korea Atomic Energy Research Institute, 898-111 Daedeok-daero, Yuseong-gu, Daejeon, 305-535, Republic of Korea
[c] Laboratory of Bio-Inspired and Graphene Nanomechanics, Department of Civil, Environmental and Mechanical Engineering, University of Trento, Via Mesiano 77, I-38123 Trento, Italy
[d] Centre for Materials and Microsystems, Fondazione Bruno Kessler, Via Sommarive 18, I-38123 Povo (Trento), Italy
[e] School of Engineering and Materials Science, Queen Mary University of London, Mile End Road, E1 4NS, London, UK

Contents

S1. Structures of symmetric and asymmetric tilt grain boundaries (GB)

* Corresponding author. Tel.: +82-42-350-3019, Fax: +82-42-350-3059.

E-mail addresses: ryush@kaist.ac.kr (S. Ryu)

The polycrystalline graphene with symmetric tilt and asymmetric tilt GB is constructed by referring to the procedures depicted in Ref. 1 and Ref. 2, respectively. We construct a series of polycrystalline graphene with a misorientation angle between 0° and 30°. The structures of symmetric and asymmetric tilt GBs at three grain misorientation angle are presented in Figs. S1(a)−(c) and Figs. S1(d)−(f), respectively. GBs, which are composed of series of 5-7 defects, are located on the center of the polycrystalline graphene.

S2. Verification of loading speed

To verify the effect of loading speed on the mechanical response of graphene sheet, a series of nanoindentation simulations are conducted under loading speed ranged from 0.02 to 0.1 Å/ps. Fig. S2 shows the force-displacement curves with respect to the loading speed of indenter for the indenter tip located on the center of pristine graphene. The maximum load and indentation load slightly increases with loading speed but the changes are not remarkable. In the remaining part of this study, the loading speed is chosen to be 0.02 Å/ps.

S3. Uniaxial and biaxial tensile simulations of pristine graphene

We performed biaxial tensile simulation in order to directly compare with the strength of the nanoindentation simulation. Before the tensile loading test, samples are initially equilibrated for 10 ps using NPT (isothermal-isobaric) ensemble at 300K. For uniaxial tensile simulations, uniaxial tension along the x-axis (perpendicular to the GBs) is applied using NPT which allows the zero pressure in the y direction to mimic the traction free boundary condition. For biaxial tensile simulations, the graphene film is stretched in both x- and y-directions until it fails completely under NVT (canonical) ensemble. Simulations boxes are stretched by pulling on both sides (LAMMPS; ref. 4 command: fix/deform). Periodic boundary condition is applied in all direction. All samples are stretched at a constant strain rate of 10^9 s^{-1}. The stress is averaged over 1 ps at each strain increment to eliminate thermal fluctuations.

Fig. S3 depicts the stress-strain curves of uniaxial and biaxial tensile simulations. The estimated strength of biaxial tensile is 105 GPa which shows good agreement with that of the

nanoindentation simulation (see Fig. 1(d)). In comparison with uniaxial tensile, Fig. S3 shows that the biaxial strength is lower than the uniaxial strength. Therefore, the strength estimated by nanoindentation can be underestimated because the graphene is subjected to equibiaxial tensile load generated by an indenter.

S4. Comparison of stress distribution between pristine and polycrystalline graphene

For comparison, indentation simulations are carried out to investigate the stress distribution of pristine and polycrystalline graphene under the same simulation conditions. The non-uniform stress distribution of pristine and symmetric tilt GB with the angle of 5.7° are plotted together which is obtained slightly before the rupture as shown in Fig. S4(a). The stress is defined by the average between σ_{xx} and σ_{yy}. We observed that the stress decreases with distance from the center of indenter tip. For the symmetric tilt GB, there is a very sharp peak in the stress distribution due to the pre-stress around 5-7 defects. A sequence of snapshots shows that rupture starts at lower indentation depth (see Fig. S4(d)).

S5. Size effect of indenter radius on mechanical response under nanoindentation

A series of nanoindentation simulations with the indenter radius of 2 nm is performed to investigate the size effect of indenter radius. We obtain the force-stress curve for the pristine graphene under nanoindentation with the same indenter radius, as shown in Fig. S5(a). The failure force is converted into the strength using the stress-force relationship. All stress-strain curves are shown in Fig. S5(b). We estimate the strength as a function of distance away from the GB line (see the inset of Fig. 5(a)). As shown in Fig. S5(c)), the failure strength approaches that of pristine graphene as the distance which becomes in close proximity to the indenter radius (~2 nm). The smaller indenter radius leads to more sharp stress concentration within the indenter radius. Hence, the strength can be overestimated at a smaller misalignment. It note that there is the prospect of high strength estimation in the case of indenter misalignment. Therefore, the estimated strength is close to that of pristine graphene at a distance of indenter radius, regardless of indenter size.

S6. Force-displacement curves of polycrystalline graphene

The force-displacement curves of polycrystalline graphene with symmetric and asymmetric tilt GBs are presented in Figs. S6 and S9. First, we examine the sensitivity of strength according to the position of the indenter by moving the location of indenter along the GB (see the inset of Fig. 3(a)). The force-displacement curves of symmetric and asymmetric tilt GBs are presented in Figs. S6 and S7, respectively. The force-displacement curve is significantly dependent on the location of the indenter. Compared to the mean value of the strength, the strength is varied by up to about 16%, the position of the indenter at low-tilt angle GBs (see Figs. 3(c) and (d)). Note that this difference is not caused by a statistical error of molecular dynamics since the difference is larger than the statistical error at each misorientation angle.

Second, in order to investigate the effect of a misaligned indenter on the strength of polycrystalline graphene, GB line is shifted from the position of indenter corresponds to the geometric center of graphene sheet (see the inset of Fig. 5(a)). The force-displacement curves of symmetric and asymmetric tilt GBs, according to the distance S, are presented in Figs. S8 and S9, respectively. We observe that the strength is proportional to the distance and approaches that of pristine graphene (see Fig. 5).

S7. Stability of crack

In the linear elastic fracture mechanics, the energy release rate for crack growth $G(a)$ is given as $\partial U / \partial a$, where ∂U is the infinitesimal change in potential energy due to the existing crack with length $2a$. Under uniaxial tension, it is known that $\Delta U = \frac{\pi a^2 \sigma_0^2 t}{E}$ where E, t and σ_0 refer to the Young's modulus, thickness, and the applied stress, respectively. Thus, the energy release rate is proportional to a, i.e. $G(a) \propto a$, and $\frac{\partial G}{\partial a} > 0$. This explains why the crack growth is unstable for uniaxial tension, as depicted in Fig. 4 (b).

On the contrary, the stress field near the indenter tip is highly concentrated around the tip. It is known that the stress field for $r < r_1$ is approximately constant where r_1 is the radius of contact area[3] (See Fig. S10). For $r > r_1$, stress field $\sigma(r)$ decays as $1/r$ because of the force balance in the vertical direction $\left(F = 2\pi r t \sigma(r) \sin\theta\right)$. Note that $\Delta U \approx \frac{\pi a^2 \sigma_0^2 t}{E}$ when $< r_1 a$. On the other hand, $\Delta U \approx \Delta U_1 + \frac{2\pi t}{E}\int_{r_1}^{a} \sigma(r)^2 r dr = \Delta U_1 + \frac{F^2}{2\pi t E \sin^2\theta} \ln\frac{a}{r_1}$ when $a > r_1$ where ΔU_1 is the potential energy change within the contact area. When a is larger than r_1, the energy release rate becomes inversely proportional to a, i.e. $G(a) \propto \frac{1}{a}$, and $\frac{\partial G}{\partial a} < 0$. Thus, crack growth becomes stable when the crack size is larger than r_1. This explains why the crack does not grow immediately after the nucleation for the low-angle GBs in Fig. 4 (a). At a small indentation depth, a crack can nucleate from the 5-7 defect where pre-stress is high, but it does not grow beyond the radius of contact r_1. r_1 increases as indentation depth increases further, which is followed by gradual crack growth. The ultimate fracture occurs once the crack size becomes comparable to the indenter radius.

For the pristine graphene or high-angle GBs, the crack nucleates at high indentation depth when stored elastic energy is very high and r_1 is comparable to indenter radius. Then, crack growth immediately up to the indenter radius, and fracture occurs simultaneously with crack nucleation, as shown in Fig. 2 (a).

References

1. Y. J. Wei, J. T. Wu, H. Q. Yin, X. H. Shi, R. G. Yang and M. Dresselhaus, Nat. Mater., 2012, 11, 759-763.

2. J. Han, S. Ryu, D. Sohn and S. Im, Carbon, 2014, 68, 250-257.

3. M. R. Begley and T. J. Mackin, J. Mech. Phys. Solids., 2004, 52, 2005-2023.

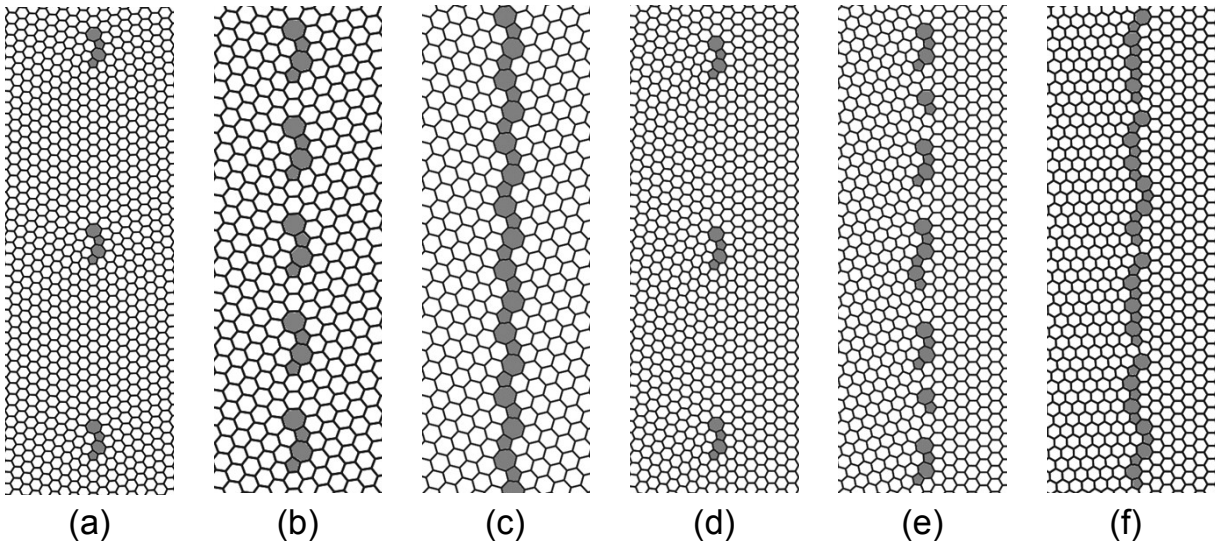

Fig. S1 – The structures of armchair-oriented graphene grain boundaries at various misorientation angles in this study. (a)-(c) Typical structures of symmetric tilt GBs: (a) 5.7˚, (b) 17.9˚, and (c) 27.8˚. (d)-(f) Typical structures of asymmetric tilt GBs: (d) 6.17˚, (e) 17.39˚, and (f) 27.0˚.

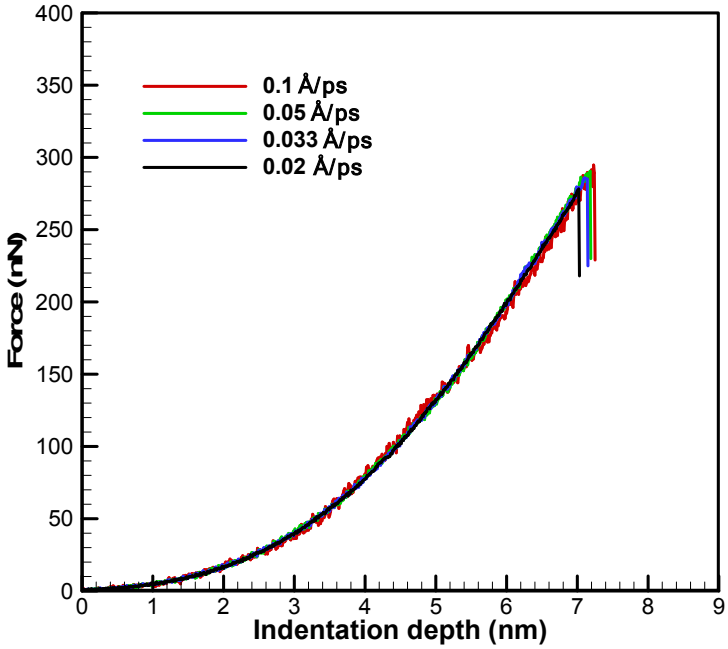

Fig. S2 – The force-displacement curves with respect to the loading speed of indenter for the indenter tip located on the center of pristine graphene.

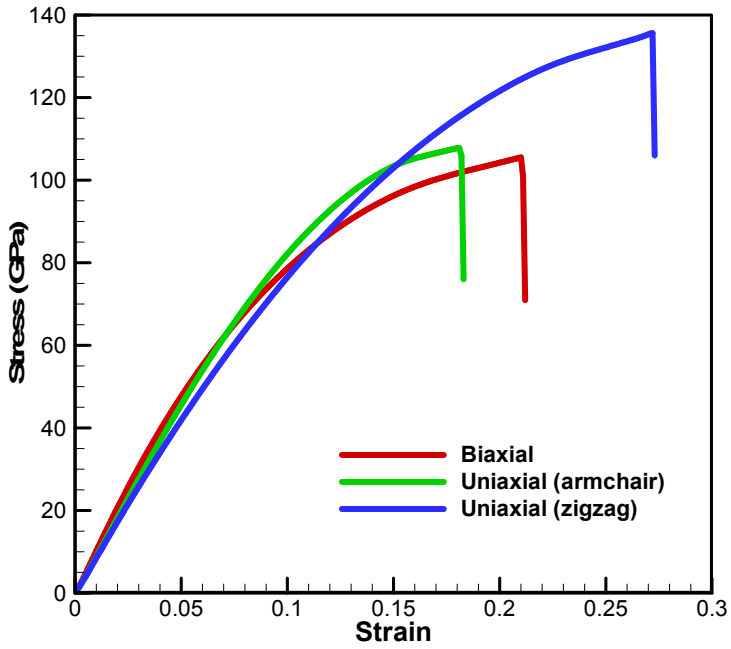

Fig. S3 – The stress-strain curves of uniaxial tensile and biaxial tensile simulations.

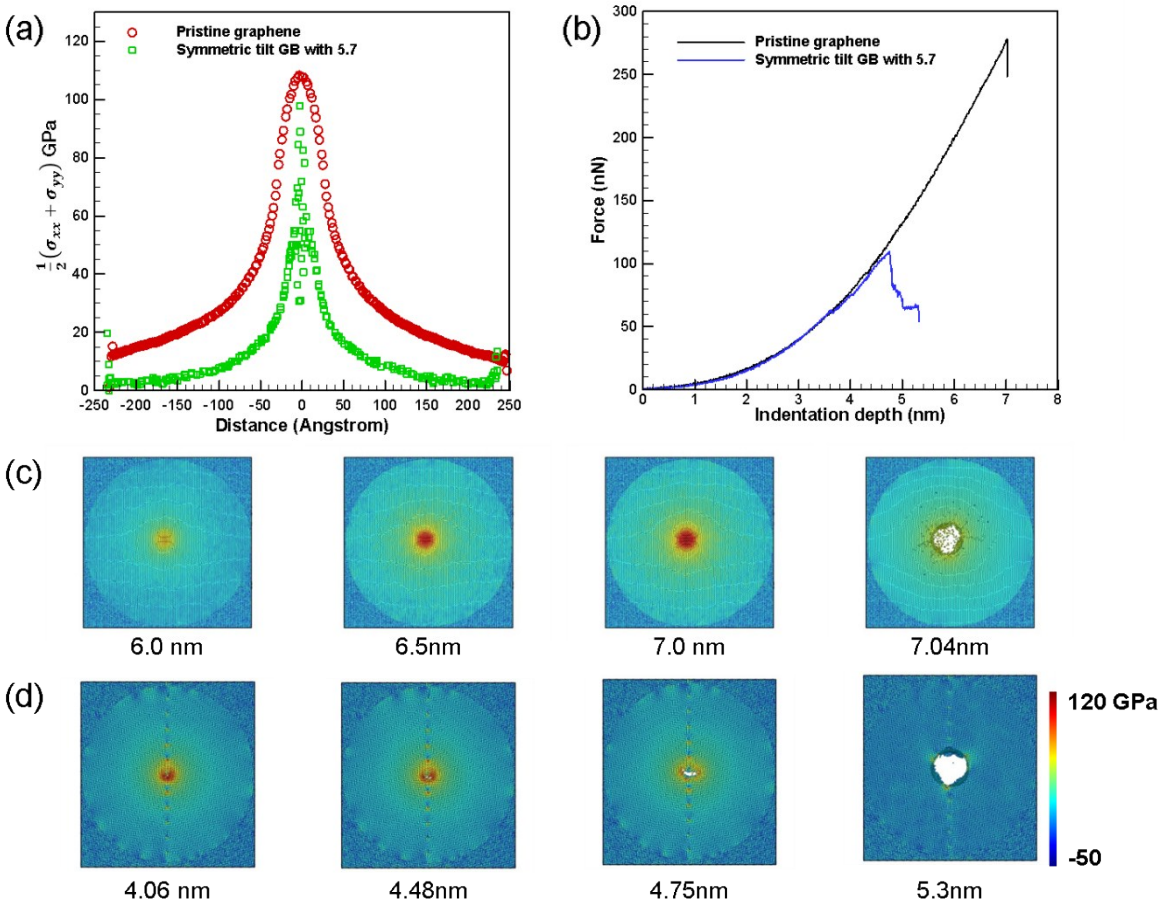

Fig. S4 – Comparison of stress distribution between pristine and bicrystal graphene. (a) In-plane stress distribution along the central line of graphene sheet on the verge of rupture. Stress represents the average between σ_{xx} and σ_{yy}. (b) Force-displacement curves of pristine and bi-crystal graphene are plotted together. The rupture process of (c) pristine graphene, and (d) symmetric tilt GB with 5.7°. The color contours indicate $\frac{1}{2}(\sigma_{xx} + \sigma_{yy})$.

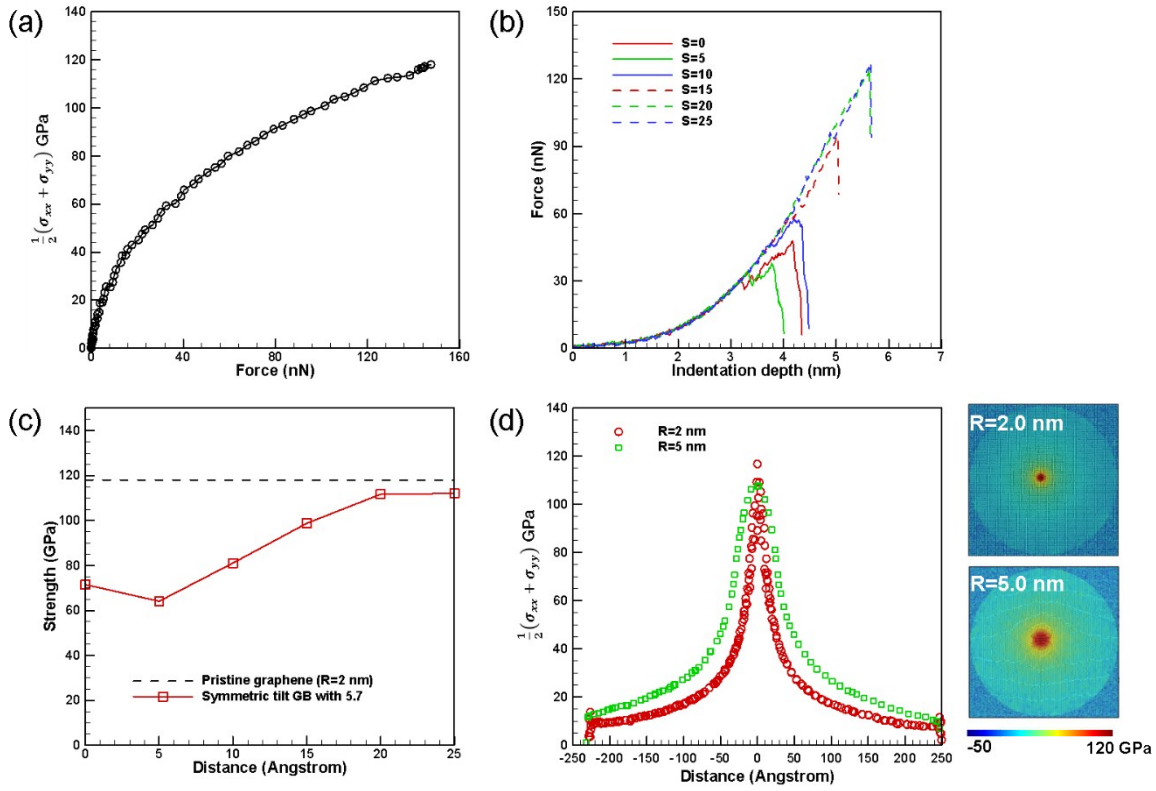

Fig. S5 – (a) Stress versus force curve for pristine graphene with the indenter radius of 5 nm. (b) The force-displacement curves of symmetric tilt GBs with various tilt angles. (c) Strength estimation as a function of indenter position (s) for symmetric tilt GB with 5.7°. (d) In-plane stress distribution along the central line of graphene sheet and atomic stress distributions on the verge of rupture. Stress represents the average between σ_{xx} and σ_{yy}. The color contours indicate the $\frac{1}{2}(\sigma_{xx} + \sigma_{yy})$.

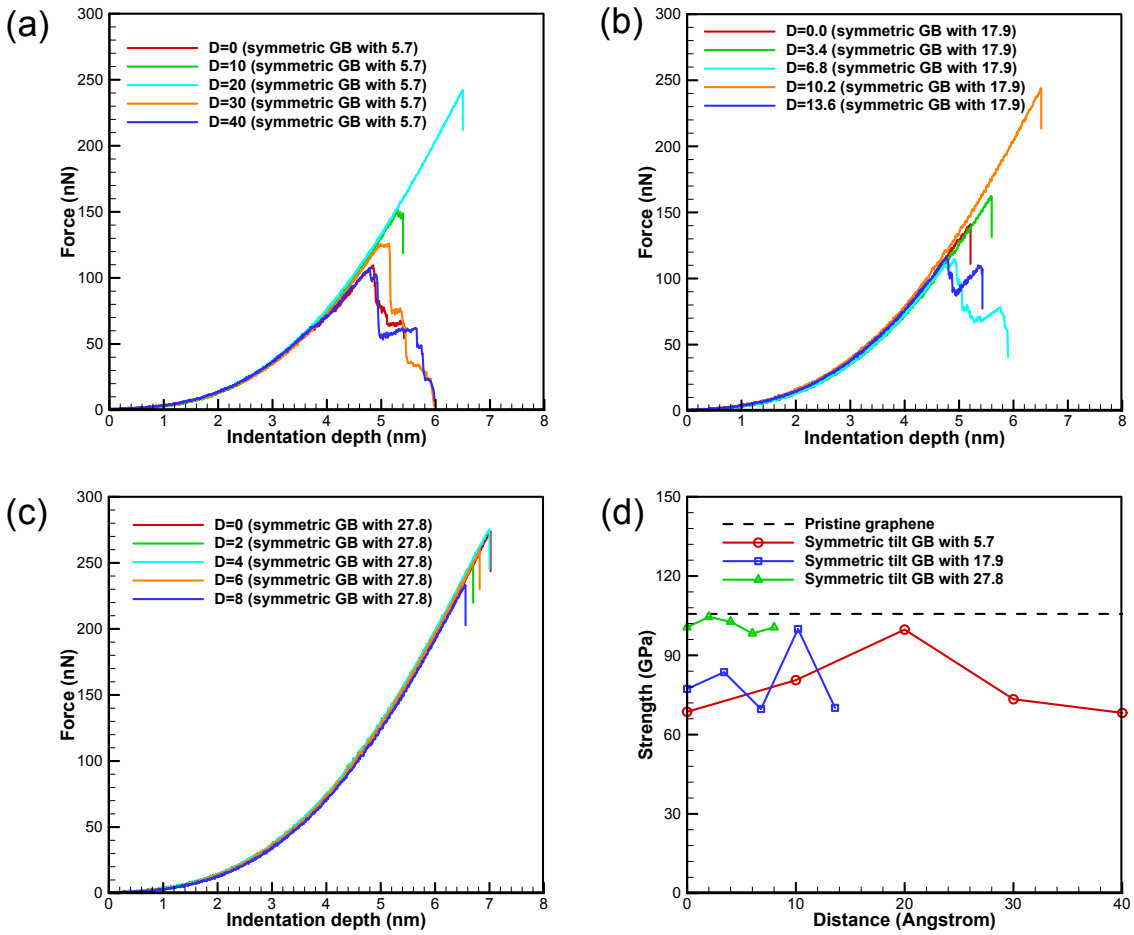

Fig. S6 – The force-displacement curves of symmetric tilt GBs with various tilt angles. The force-displacement curves of symmetric tilt GBs with respect to indenter location along the GB line: (a) 5.7˚, (b) 17.9 ˚, and (c) 27.8 ˚.

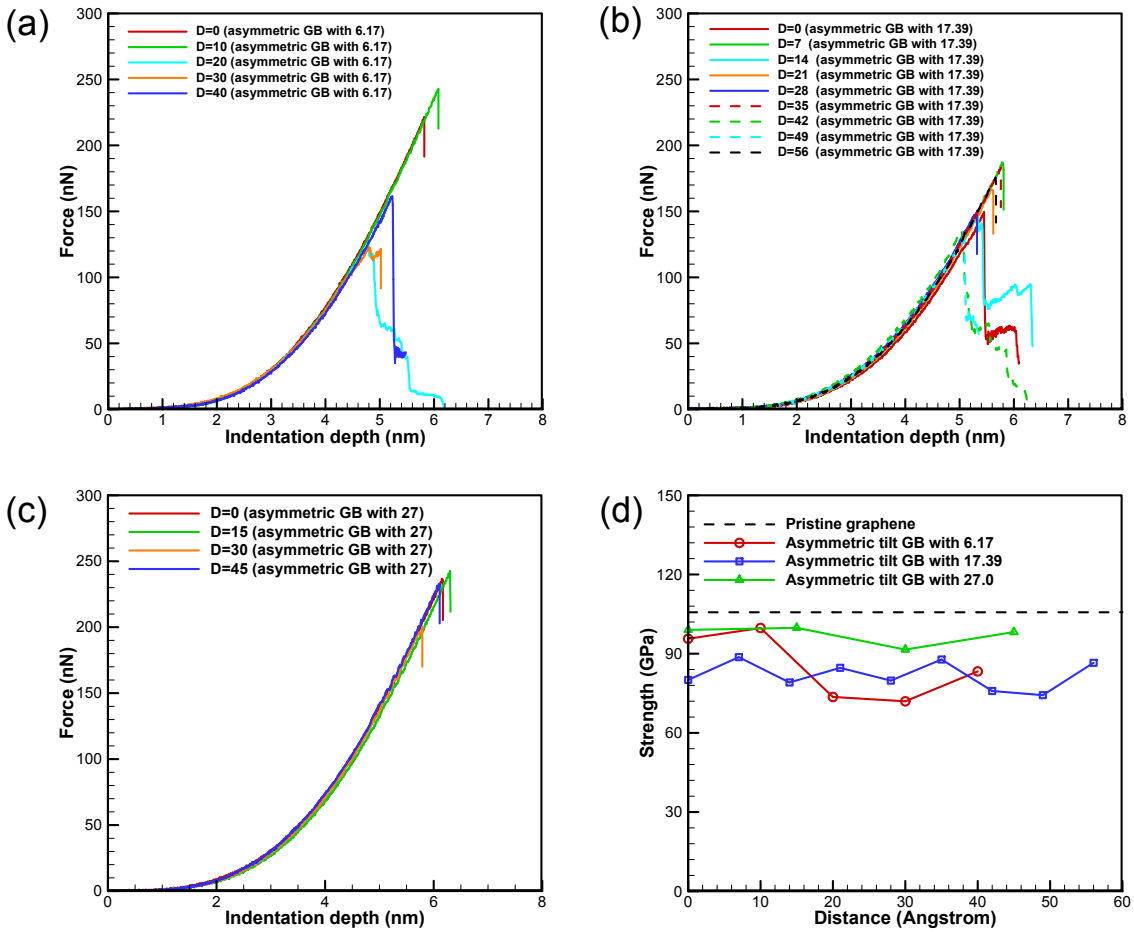

Fig. S7 – The force-displacement curves of asymmetric tilt GBs with various tilt angles. The force-displacement curves of asymmetric tilt GBs with respect to indenter location along the GB line: (a) 6.17˚, (b) 17.39 ˚, and (c) 27˚.

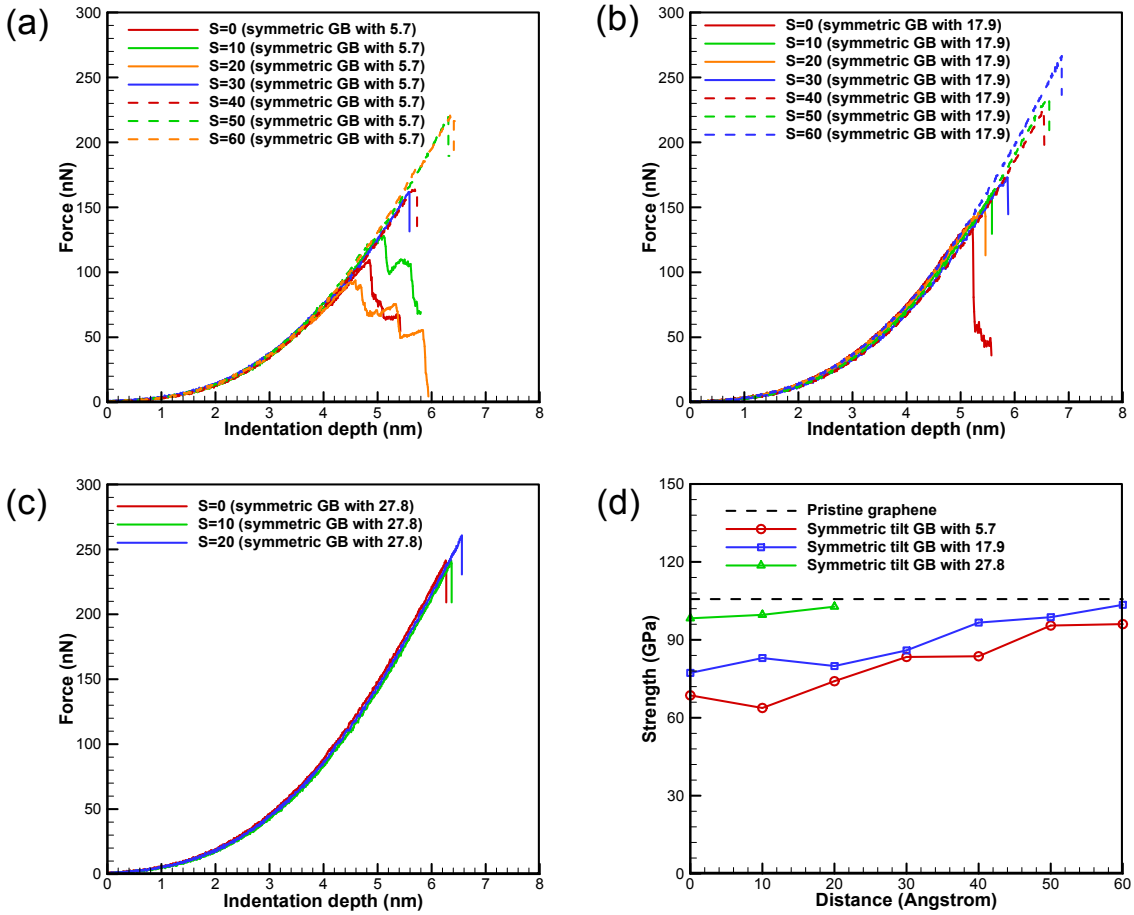

Fig. S8 – The force-displacement curves of symmetric tilt GBs with various tilt angles. The force-displacement curves of symmetric tilt GBs with respect to the distance S: (a) 5.7˚, (b) 17.9 ˚, and (c) 27.8˚.

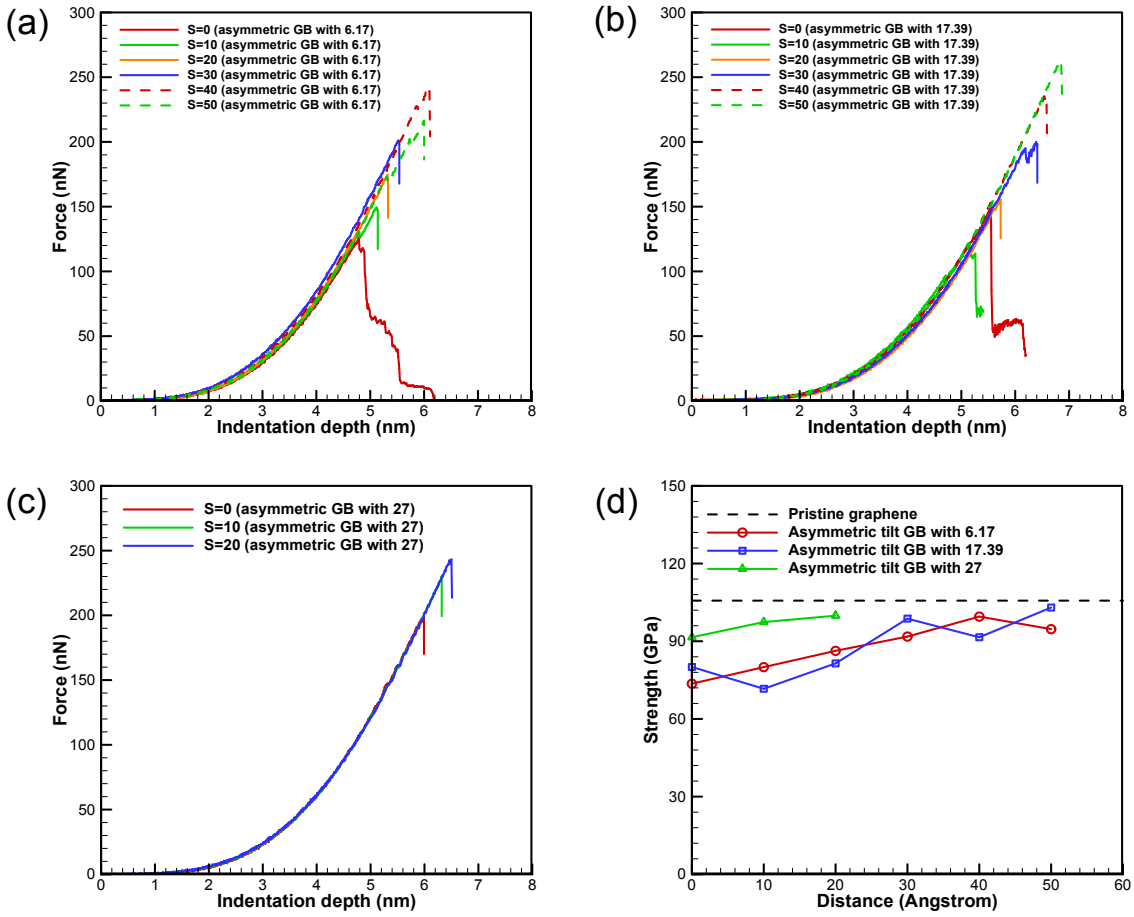

Fig. S9 – The force-displacement curves of asymmetric tilt GBs with various tilt angles. The force-displacement curves of asymmetric tilt GBs with respect to the distance S: (a) 6.17˚, (b) 17.39 ˚, and (c) 27˚.

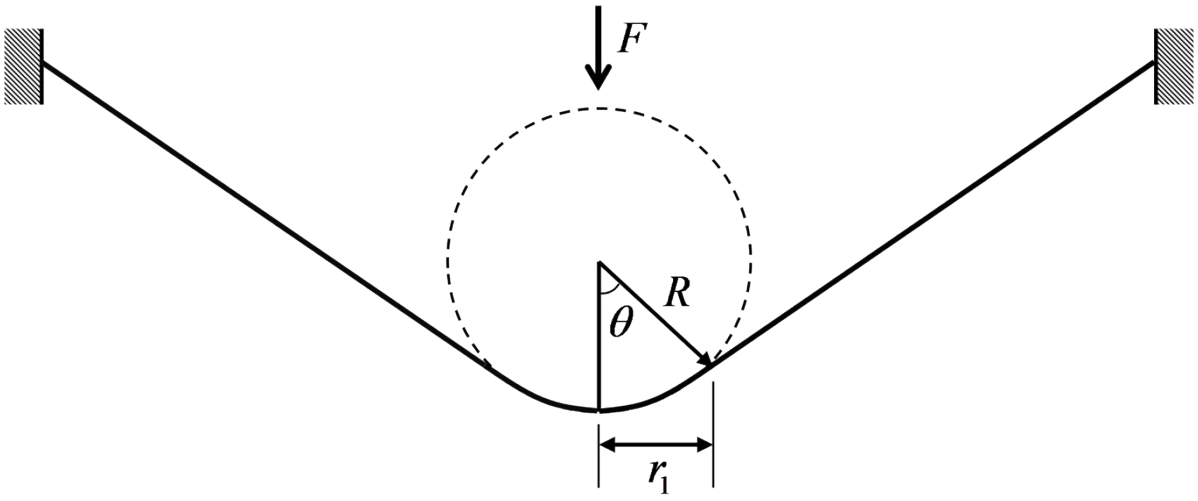

Fig. S10 – Schematic diagram of a spherical indenter with polycrystalline graphene.